Fatigue life and cracking characterization of engineered cementitious composites (ECC) under flexural cyclic load

Sun, Renjuan; Han, Lebing ; Zhang, Hongzhi; Ge, Zhi; Guan, Yanhua ; Ling, Yifeng ; Schlangen, Erik; Šavija, Branko

DOI
10.1016/j.conbuildmat.2022.127465

Publication date
2022

Document Version
Final published version

Published in
Construction and Building Materials

Citation (APA)
Sun, R., Han, L., Zhang, H., Ge, Z., Guan, Y., Ling, Y., Schlangen, E., & Šavija, B. (2022). Fatigue life and cracking characterization of engineered cementitious composites (ECC) under flexural cyclic load. *Construction and Building Materials*, *335*, 1-14. Article 127465. https://doi.org/10.1016/j.conbuildmat.2022.127465

Construction and Building Materials 335 (2022) 127465

Contents lists available at ScienceDirect

Construction and Building Materials

journal homepage: www.elsevier.com/locate/conbuildmat

Fatigue life and cracking characterization of engineered cementitious composites (ECC) under flexural cyclic load

Renjuan Sun [a], Lebing Han [b], Hongzhi Zhang [a,c,*], Zhi Ge [a,*], Yanhua Guan [a], Yifeng Ling [a], Erik Schlangen [d], Branko Šavija [d]

[a] School of Qilu Transportation, Shandong University, 250002 Jinan, PR China
[b] Shandong Hi-Speed Engineering Test CO., LTD, 250002 Jian, PR China
[c] Suzhou Research Institute, Shandong University, 215021 Suzhou, PR China
[d] Microlab, Faculty of Civil Engineering and Geosciences, Delft University of Technology, 2628 CN Delft, the Netherlands

ARTICLE INFO

Keywords:
Fatigue life
Engineered cementitious composites
Digital image correlation
Cracking behavior

ABSTRACT

This paper presents a study on cracking characterization of engineered cementitious composites (ECC) under flexural cyclic load using digital image correlation (DIC) technique. Five stress levels, namely 0.65, 0.75, 0.8, 0.85 and 0.9 of the flexural strength, were applied. Strain map at the side surface was obtained by DIC and used to drive evolution of the midspan deflection, damage pattern, maximum crack width, number of cracks, and crack width distribution with respect to the normalized number of cycles. The stress level was found to have a significant influence on the cracking behavior of ECC under flexural cyclic load. Regardless of the applied stress level, most of the crack widths are in the range between 20 and 80 μm. In the end, a two-dimension Gauss function was used to correlate the crack width distribution with normalized number of cycle and shows satisfactory results.

1. Introduction

Engineered cementitious composites (ECCs) belong to a broad class of fiber reinforced concrete [1]. They are sometimes also termed as strain-hardening cementitious composites (SHCCs) or ultra-high toughness cementitious composites (UHTCCs). ECCs are a family of cementitious materials with the common feature of being ductile, with tensile strain capacity typically beyond 2% [2–4]. ECC design is based on engineering the fiber, matrix, and fiber/matrix interface features deliberately to improve the tensile deformation capacity of the composite. Under monotonic tensile loading, multiple microcracks develop along the ECC specimen, instead of localized fracture typically found in conventional concrete. Consequently, ECC possesses a metal-like stress–strain response, in which strain-hardening occurs after a distinctive "yield" strength. The tensile ductility, the strain capacity at peak strength, of ECC is typically two orders of magnitude higher than that of normal concrete [5]. This allows the flexural strength of ECC to reach 10–15 MPa, 2–3 times that of conventional concrete [6]. The tight crack width of ECC (generally <100 μm [7]) allows the material to possess a significant ability to recover mechanical properties through autogenous healing in the presence of water [8–11].

Unlike the fracture behavior under monotonic loading, fatigue fracture of ECC is a process of progressive, permanent internal structural changes, which inevitably result in the changes of the performance of ECC with time [7]. Therefore, it is important to have an in-depth understanding of the fatigue behavior of ECC for structural design and service life estimation. Similar to concrete, the fatigue performance of ECC can be characterized by an *S-N* curve, in which the amplitude of the cyclic stress (*S*) is related to the number of cycles to failure (*N*). ECC has a much longer fatigue life at high stress level compared to plain concrete, polymer cement mortar, and steel fiber-reinforced concrete, due to the fiber-bridging effect [12–14]. However, with the fatigue stress level decreasing, a reduction in number of cracks has been observed by Matsumoto and Kanda [15,16]. Through microscopic investigation of fracture surfaces, Müller and Mechtcherine [17] demonstrated that the decrease in strain capacity under fatigue loading in uniaxial tension can be traced back to less pronounced or even absent multiple cracking and to the transition of the failure mode from fiber pull-out to fiber failure. Huang et al. [18,19] investigated the fatigue failure of ECC under compression. Three type of fatigue-induced fiber failure modes, namely,

* Corresponding authors at: School of Qilu Transportation, Shandong University, 250002 Jinan, PR China (H. Zhang and Z. Ge).
E-mail addresses: hzzhang@sdu.edu.cn (H. Zhang), zhige@sdu.edu.cn (Z. Ge).

https://doi.org/10.1016/j.conbuildmat.2022.127465
Received 7 October 2021; Received in revised form 9 April 2022; Accepted 9 April 2022
Available online 19 April 2022

Table 1
Mix proportion of ECC, in kg/m^3 [35].

Cement	Fly ash	Quartz sand	Water	VMA	Superplasticizer	Fiber
593	712	474	339	0.59	5.22	26.0

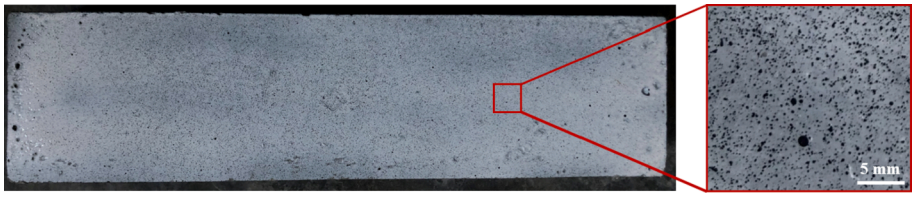

Fig. 1. Random speckle pattern obtained by black paint spray.

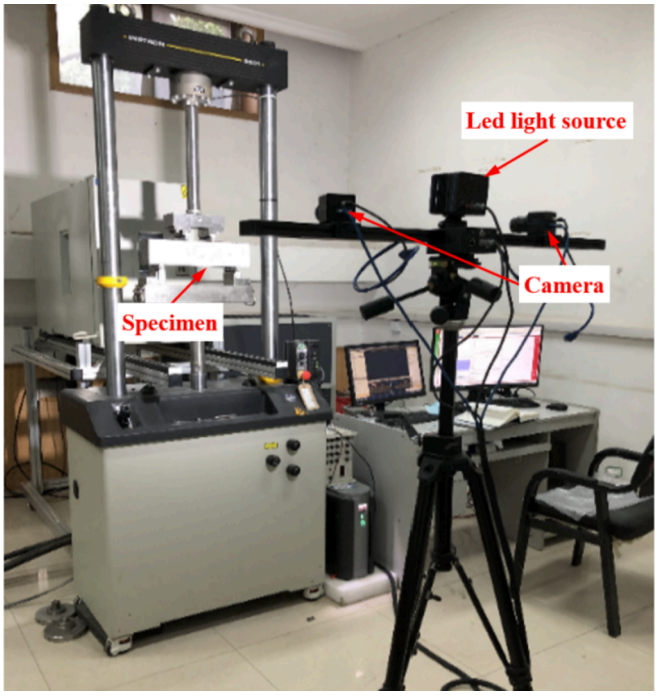

Fig. 2. DIC setup for the flexural fatigue test.

crushing, rupturing and pulling-out were observed. Furthermore, X-ray computed tomography shows that the fatigue load can cause the interior multiple cracking [20]. Microscopic studies have revealed that the fatigue-induced fiber debonding, interface hardening, and in-situ fiber strength reduction contribute to the fatigue deterioration of fiber bridging of ECC leading to failure of the ECC [21]. A micromechanical model was therefore proposed to investigate the fatigue deterioration mechanism [21–23]. On the other hand, continuum damage mechanics theory has been used to build the fatigue damage model to compute the fatigue life, fatigue crack propagation as well as the fatigue damage [24–26]. Based on the Weibull function, the fatigue life can also be predicted using a deformation based model [27].

Although fatigue performance of ECC has been extensively investigated, little effort has been put on understanding the crack pattern evolution of ECC under the fatigue loading, which plays a dominating role on assessing the durability of ECC material and structural elements. To this end, this work aims at understanding the crack evolution of ECC under flexural fatigue loading with the aid of digital image correlation (DIC) technique, which has recently been adopted to trace the evolution of crack pattern and crack width distribution of plain cementitious materials [28–30], ECC [31–33] and ECC/normal concrete hybrid systems[34] under monotonic loading. This technique is promising for studying the fatigue crack pattern evolution of ECC as it allows successive measurement of multiple cracks simultaneously during the test, and can provide more precise measurement of the crack width compared with the techniques using linear variable differential transformer (LVDT) and strain gages in which the elastic deformation of the uncracked area cannot be fully excluded from the measurement. Furthermore, if multiple cracks form inside the gauge length of LVDT or strain

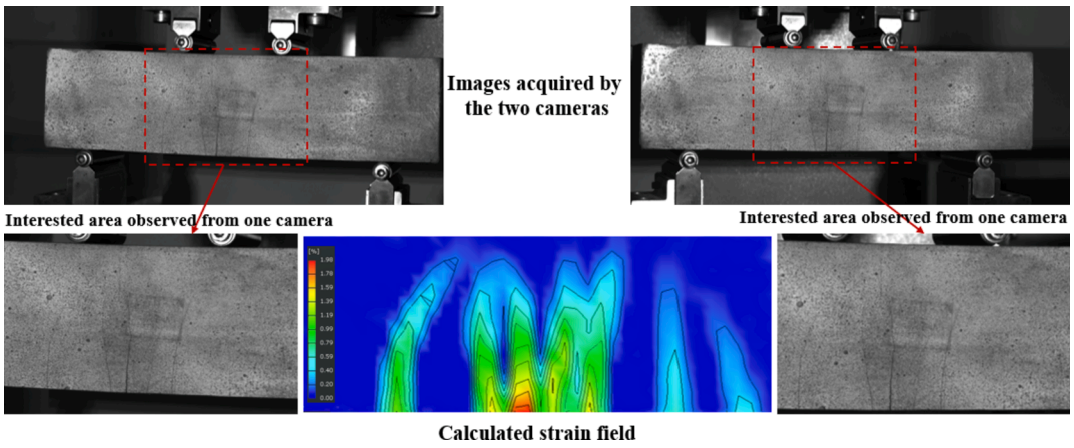

Fig. 3. Comparison between the cracked specimen and strain map obtained using DIC.

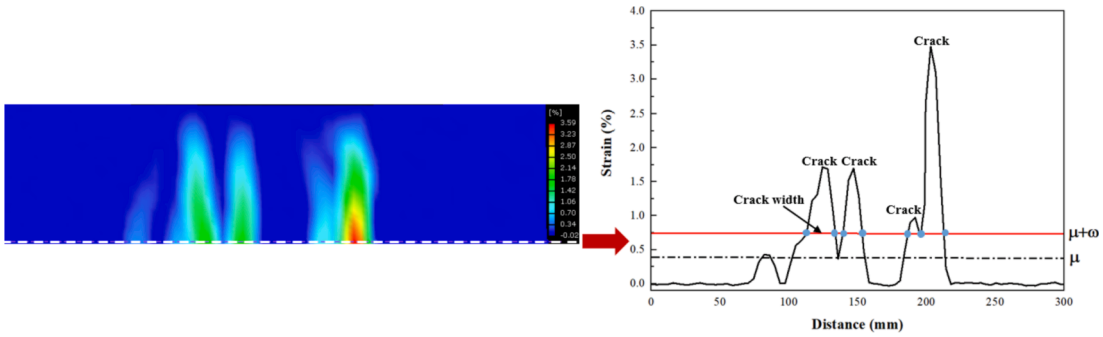

Fig. 4. Crack width determination using DIC.

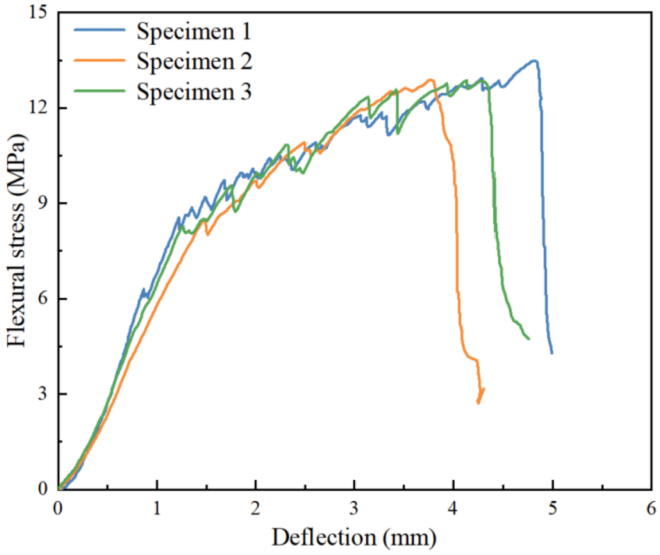

Fig. 5. Load-deflection relationship of ECC under monotonic flexural test.

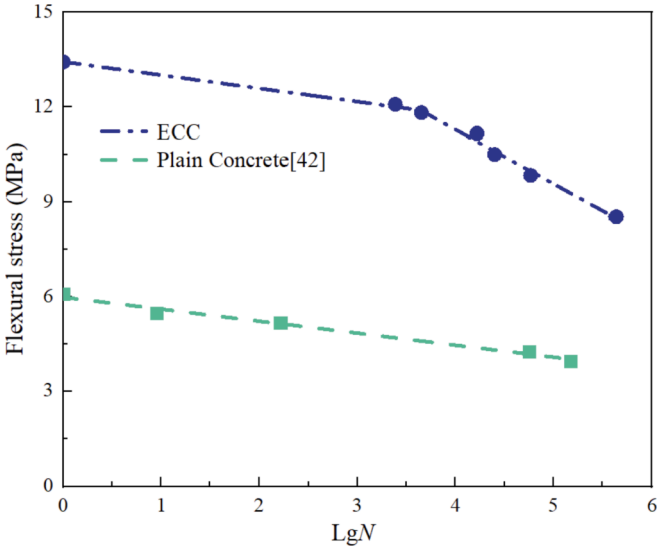

Fig. 6. Fatigue stress–life relationship comparison between ECC and plain concrete [45].

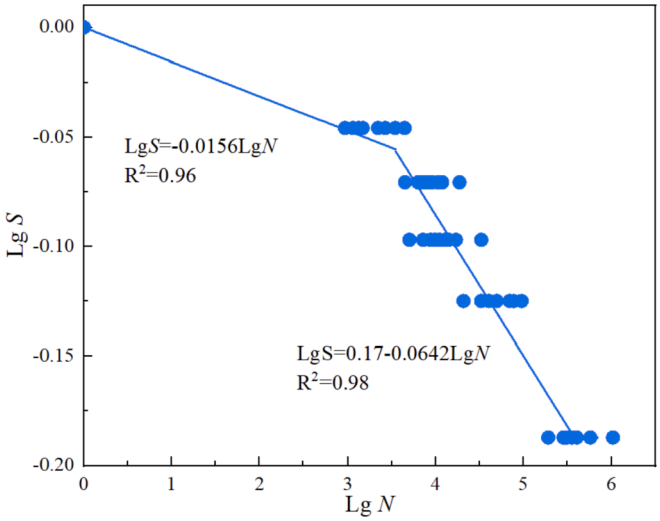

Fig. 7. Fitting of the normalized *S–N* relationship.

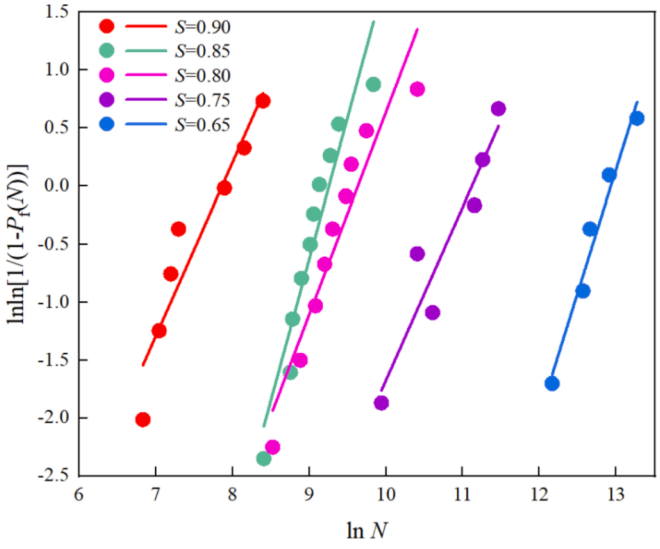

Fig. 8. Weibull plot for the fatigue life under various loading stress levels.

gages, only total crack width can be measured. Using the stain field information obtained by DIC, the evolution of the number of cracks, maximum crack width and crack width distribution on the observed surface (i.e. lateral side of the beam) along with the fatigue loading was determined. The influence of fatigue stress level (0.65, 0.75, 0.8, 0.85,

Table 2
Weibull analysis of the fatigue life under each fatigue stress level.

Stress level, S	α	N_α	R^2
0.90	1.50	2540	0.9006
0.85	2.44	10,404	0.9112
0.80	1.74	15,512	0.9134
0.75	1.5	64,000	0.9054
0.65	2.12	418,066	0.9617

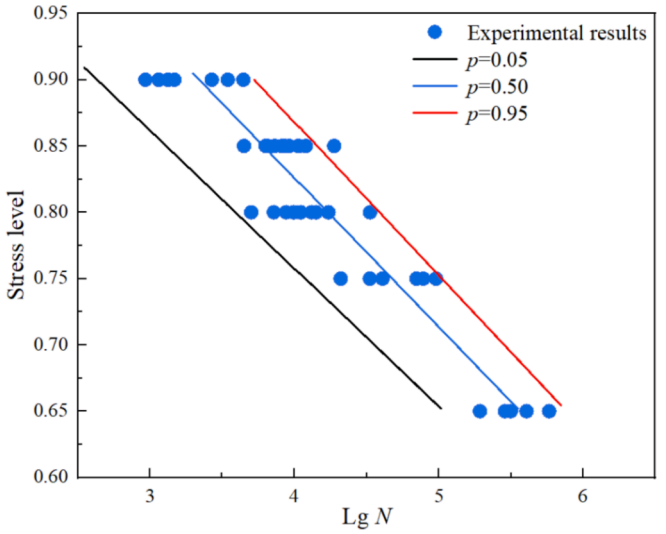

Fig. 9. Comparison between the measurements and theoretical fatigue life with varying failure probability, p.

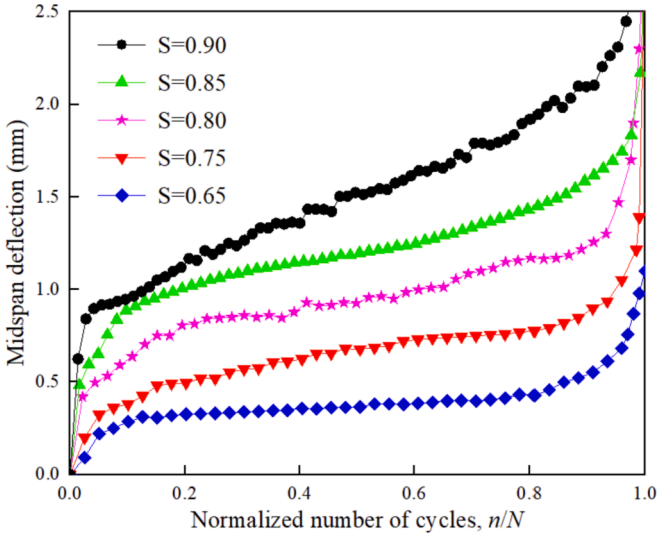

Fig. 10. Midspan deflection evolution with respect to the normalized number of cycles.

0.9 of the flexural strength) on the fracture behavior was investigated. The current study offers additional insight into the fatigue fracture behavior of ECC, thus providing a basis for durability assessment and design of ECC structures.

2. Materials and methods

2.1. Materials

Ordinary Portland cement 42.5 (Shandong Shanshui Cement Group, China), local Class-F fly ash, quartz sand with particle size of 125–180 μm and PVA fiber (Kuraray, Japan) were used. The fly ash to cement weight ratio was 1.2 and the water to binder ratio was 0.26. The fiber volume fraction is 2%. Besides, polycarboxylate ether-based superplasticizer and viscosity modifying admixture (VMA) were added to adjust the fresh properties for casting. The mix proportion of the tested ECC are present in Table 1[35]. The 28-day compressive strength and the Young's modulus of ECC measured on prismatic specimens (150 mm × 150 mm × 300 mm) were 52.3 MPa and 18.9 GPa, respectively. The four-point bending test on the thin slab ECC specimens (350 mm × 50 mm × 15 mm) showed that the first cracking strength, ultimate flexural strength and ultimate midspan deflection were 4.6 MPa, 15.5 MPa and 30.2 mm, respectively.

2.2. Specimen preparation

Specimens with the dimensions of 100 mm × 100 mm × 400 mm were cast for the flexural fatigue test. A 20L horizontal shaft mixer was used for the mixing. Cement, fly ash, quartz sand and VMA were first mixed for two minutes. Water and superplasticizer were then added to the mixture and mixed under medium speed for 4 min. Afterwards, fibers were added with low mixing speed. This procedure was completed within one minute. The mixing was resumed for another 3 min mixing at medium speed. This was followed by pouring the fresh mixture into the molds and covering with a plastic membrane. One day after the casting, the hardened specimens were demolded and subsequently cured (temperature: 20 °C; relative humidity: 95%) up to 28 days. Before the monotonic and fatigue test, the specimens were stored in the laboratory environment (temperature: 23 ± 3 °C; relative humidity: 60 ± 5%) for 3 months. For the fatigue test, digital image correlation technique (DIC) was used to capture the surface strain map within the region of interest. Therefore, random speckle patterns were made over the specimen surface using white and black spray paint. The surface was first polished using sand paper and painted with matte white paint. The dark speckle pattern was randomly sprayed on the flat white surface, see Fig. 1. This allows each subset to have a unique grey scale distribution.

2.3. Testing configuration

The monotonic and fatigue flexural tests were conducted by a MTS810 electro-hydraulic universal testing machine with a 100 kN capacity. The specimens were subjected to four-point bending. The loading span and the support span were 100 mm and 300 mm, respectively. Three specimens were tested under monotonic flexural load. Defection control with a loading rate of 0.01 mm/s was used. The average ultimate flexural strength obtained from the monotonic tests was then used to calculate the applied load for the fatigue test. In the fatigue test, load control was used. The specimen was first loaded 3 times with 0.4 time of the desired load level to ensure a tight contact between the roller and the specimen. 5 Hz sinusoidal cyclic load with a maximum value, P_{max} and the minimum value, P_{min}, was then applied. The ratio between P_{min} and P_{max} was set to 0.1. This set up can avoid impact and slip of specimen during the fatigue testing. Multiple stress levels, S, defined by Eq.(1), namely 0.90, 0.85, 0.80, 0.75 and 0.65 were used.

$$S = \frac{P_{max}}{P_{ult}} \tag{1}$$

where P_{ult} is the monotonic ultimate load of the specimen. The experiment was terminated either after failure occurred (complete fracture of the specimen) or 2×10^6 cycles were reached. After the fatigue test, an

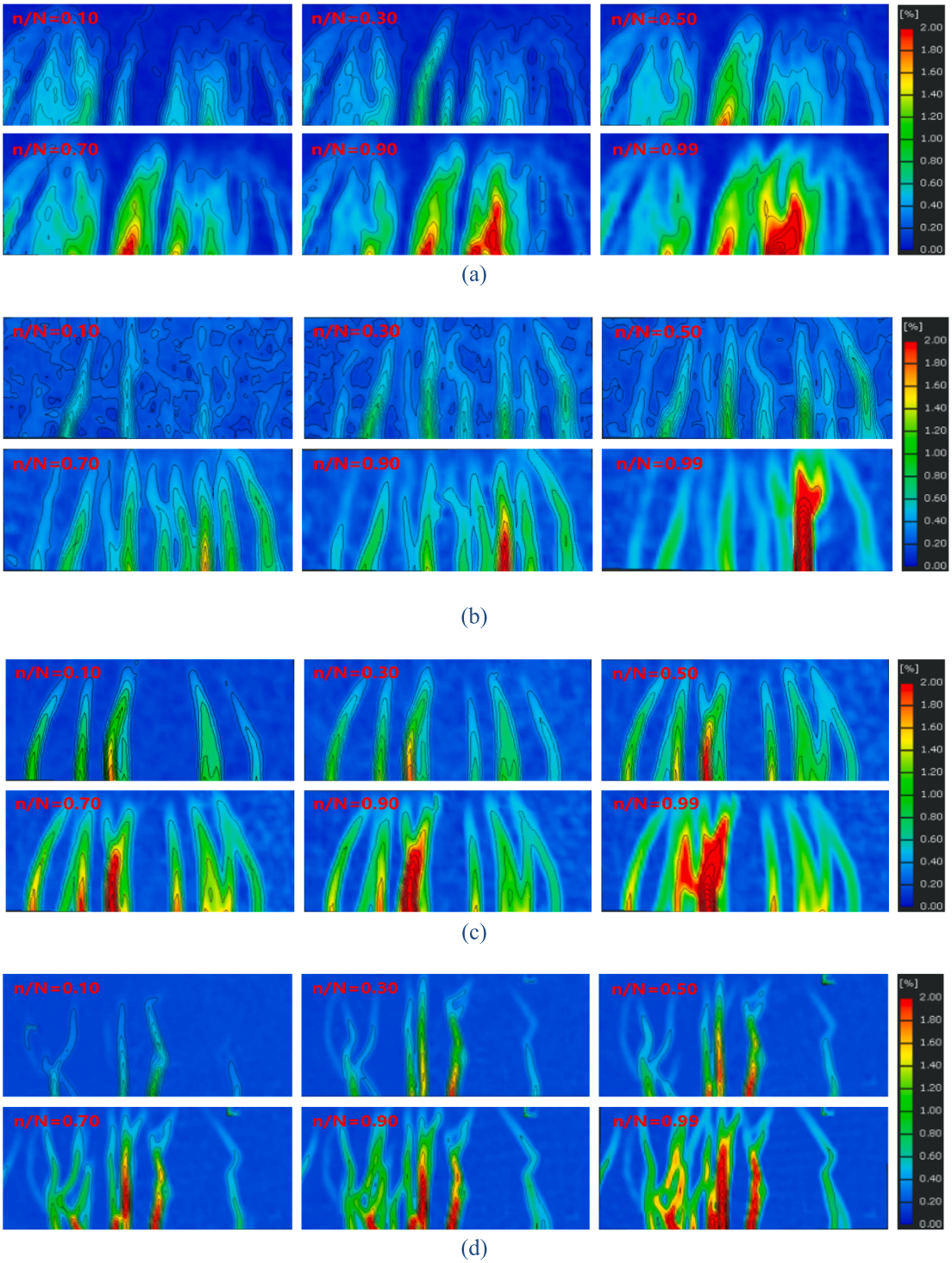

Fig. 11. Strain field evolution of specimens under the fatigue tests with stress levels of: (a) 0.9; (b) 0.85; (c) 0.80; (d) 075 and (e) 0.65 (n/N represents normalized number of cycle).

optical microscope was used to observe the exposed fibers at the fractured surface.

2.4. Crack detection using DIC

To trace the crack width development at the side of the ECC specimen, DIC technique was used. It is a non-contact optical-numerical measurement method to provide full field surface strain/displacement maps. The full field strain/displacement maps are remarkably useful when studying the behavior of cementitious materials, due to the complexity of these materials and the influence of concentration of localized strains on the behavior [36–41]. In this technique, digital images of unreformed and deformed states are captured and compared in terms of the grey level of each pixel. Small regions (termed as subsets) consisting of a set of pixels are tracked before and after deformation by matching their grey scale distribution. The displacement/strain field is

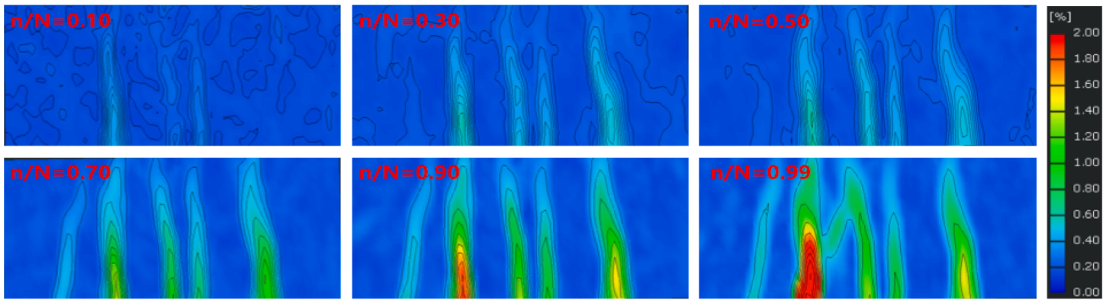

(e)

Fig. 11. (*continued*).

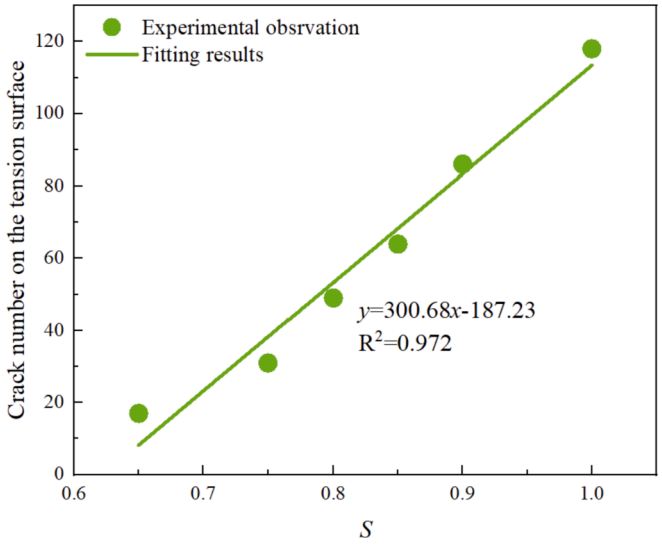

Fig. 12. Relationship between the crack number on the tension face and stress level at the failure stage.

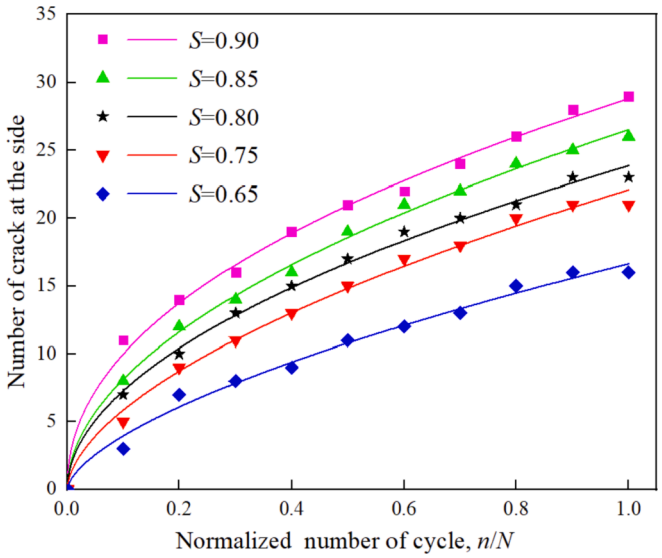

Fig. 13. Evolution of the observed number of cracks at the side with the normalized number of cycles.

Table 3
Relationship between crack number and normalized number of cycles under each fatigue stress level.

Stress level, S	a	b	R^2
0.90	28.80	0.46	0.974
0.85	26.51	0.51	0.966
0.80	23.86	0.52	0.992
0.75	22.09	0.58	0.987
0.65	16.37	0.62	0.993

then computed from the movement of subsets.

A 3D full-field strain measurement system developed by Xian Xintuo Company was used for image acquisition and analysis. The Image acquisition system consists of two high-precision 8-bit TAWOV cameras. The cameras have a spatial resolution of 2448 × 2048 and a graphic resolution of 5 megapixels. Cameras were mounted on a tripod and placed 1 m from the tested specimen, see Fig. 2. With this setup, the resolution of the image is 3.5 μm × 3.5 μm/pixel. Digital images were taken every second when the specimen was loaded. Prior to the test, cameras were calibrated for its position and orientation using a calibration grid plate. In this process, the calibration grid plate was placed in the same plane as that of the CCD chip of the camera and at a same distance as that of the specimen. After the calibration, DIC system can translate the image coordinate to geometric coordinate accurately. More details about the calibration process can be found in [42].

For the strain calculation, the subset dimension and step size were chosen as 20 × 20 pixels and 20 pixels, respectively. This set up is capable of providing a displacement with an accuracy of 1/50 pixel [43]. Fig. 3 compares the calculated strain filed and the cracked specimens at a certain stage. Clearly, each counter of the strain peak corresponds to a single crack. To trace the crack automatically, an approach by Ruocci et al. [44] was adopt. In this approach, crack points were recognized by analyzing the horizontal measuring line at the outmost of the tension side. As shown in Fig. 4, strain peaks are treated as crack points once they exceed a threshold value. In general, the threshold value is defined as the mean value plus one standard deviation (μ + ω) of the longitudinal strain distribution in the measuring line. The crack widths can be derived on the basis of the displacement field information of two reference points at the left- and right-hand side of the crack point location. The crack points were then clustered and traced. In this way, the crack width development and the number of cracks can be recorded.

3. Results and discussions

3.1. Monotonic flexural test

Monotonic load–deflection curve of the measured specimens is plotted in Fig. 5. As expected, deflection hardening behavior is observed attributed to multiple cracking characteristic generated by the fiber bridging effect. The average ultimate load is 44.75 kN with a standard

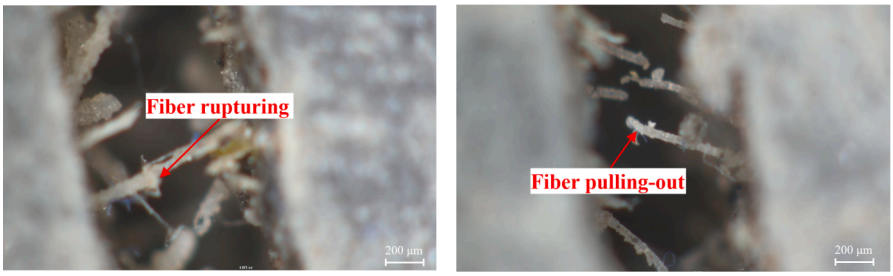

(a) (b)

Fig. 14. Microscopic image of PVA fiber on the fracture surface of specimens under (a) stress level of 0.65 in which most of the fibers are ruptured and (b) stress level of 0.9 in which most of the fibers are pulled-out.

deviation of 1.14, corresponding to a strength of 13.45 ± 0.43 MPa. The applied P_{max} for fatigue test was there therefore determined as 40.28, 38.04, 35.80, 33.56 and 29.09 kN, respectively, for $S = 0.90$, 0.85, 0.80, 0.75 and 0.65.

3.2. Fatigue stress–life relationship

The results of fatigue tests under various P_{max} are presented in Fig. 6 and compared with plain concrete. It is evident that ECC has much stronger fatigue load resistance than plain concrete for a certain fatigue life. Similar to the observation in Ref [13], a bilinear *S-N* relation, such as that of metallic materials, is observed for ECC. Note that, with fatigue cycle increasing, a faster decrease in fatigue flexural strength is observed compared with plain concrete [45].

To determine the *S-N* relationship, the stress level, S is plotted together with cycles to failure, N in Fig. 7. To meet the following two boundary conditions: (1) $N = 1$ when $S = 1$ and (2) $N \to \infty$ when $S \to \infty$, a double logarithmic equation in the form of $\mathrm{Lg}S = \mathrm{LgA} - B\mathrm{lg}N$ was adopted in which A and B are fitting parameters. As can be seen, the bilinear double logarithmic fatigue equation can describe the *S-N* relationship well, with determination coefficients above 0.95 for both branches. The inflection point is positioned between $\mathrm{Lg}N = 3$ and 4. As pointed by Li et al. [46], the double logarithmic equation can be used for the prediction. Assuming $N = 2 \times 10^6$ as the fatigue limit, a corresponding stress level, $S = 0.5921$ is obtained. This agrees with the experimental observation in Ref [13].

3.3. Weibull analysis of fatigue life

Similar to concrete, ECC shows large variability in fatigue test results. This should be considered in the design of ECC. Therefore, statistic-based approaches should be applied. Weibull distribution has been widely applied for characterization the fatigue life of plain and fiber reinforced concrete [45–49]. Herein, a two-parameter Weibull distribution was adopted:

$$\ln\ln\frac{1}{1-P_f(N)} = \alpha\ln N - \alpha\ln N_a \tag{2}$$

where $P_f(N)$ is the cumulative probability of failure; α is the shape parameter describing the variability; N_a is the scale parameter (characteristic fatigue life). The characteristic fatigue life corresponding to a failure probability of 0.63, which means that, statistically, 63 % of specimens fails at the characteristic fatigue life.

According to the probability theory of Weibull distribution, the failure probability, p corresponding to the failure life N can be expressed by:

$$p = \frac{i}{k+1} \tag{3}$$

where k is the total number of fatigue test data at certain S, i the sequence number of failure specimens at certain S. The cycles to failure for each S are plotted in a Weibull coordinate system, see Fig. 8. The least-squares method was performed to obtain α and N_a. Table 2 shows the fitting results. It is evident that all correlation coefficients are above 0.90. This validates that the fatigue life of ECC follows the double-parameter Weibull distribution. Fig. 9 compares the measurements and theoretical fatigue life with varying failure probabilities. Most of the experimental results are within the failure probability between 5% and 95%, except one at the stress level of 0.85.

3.4. Evolution of midspan deflection under fatigue load

The midspan deflection evolution was derived from DIC analysis and plotted against the normalized number of cycles in Fig. 10. Similar to the observation in Ref. [13] where an LVDT was used for the measurement, the evolution of midspan deflection depends on the fatigue stress level. Under $S = 0.9$, the midspan defection under fatigue loading can be higher than 2 mm, which is more than two times that of the specimens under $S = 0.65$. Furthermore, three stages can be distinguished from the midspan defection evolution diagram. Similar observations have been reported for hydrated cement paste at the micro-scale [50]. In the first stage ($n/N < 0.1$), the deflection grows with the normalized number of cycles. Afterwards, the increase rate reduces remarkably and remains nearly constant before $n/N < 0.8$. This is followed by a rapid increase at stage III. The increment is more significant for the specimens under lower fatigue stress levels. Mechanisms responsible for this behavior are described below.

3.5. Strain field evolution under fatigue load

The evolution of the strain field of ECC with respect to the normalized number of cycles to failure is shown in Fig. 11. For each stress level, strain fields at 6 different failure stages are plotted. It is clear that the area with strain concentration increases with the number of load cycles. This means that the damaged area expends with the cycle. Assuming that the strain concentration area corresponds to the damage or a crack, one can observe that multiple cracks initiate from the bottom at stage $n/N = 0.1$ and tend to propagate to the top and increase their width gradually. It is worth mentioning that during this deterioration process, although some new cracks do form, the major cracks that lead to failure are among those observed already at $n/N = 0.1$. This indicates that in general the failure is caused by crack growth, rather than the initiation of new cracks under the flexural cyclic load.

Furthermore, the strain concentration (damaged) area is sensitive to the applied stress. Compared with the specimens under high stress level, cracks initiated in specimens under low stress level tend to propagate to the top rather than extending in width. When $S = 0.65$, the damage is more localized, and only several narrow and localized strain branches are observed. With the fatigue stress level increasing, more strain concentration (damaged) branches are observed, and some of them coalesce as the number of load cycles increases. This can be attributed to the

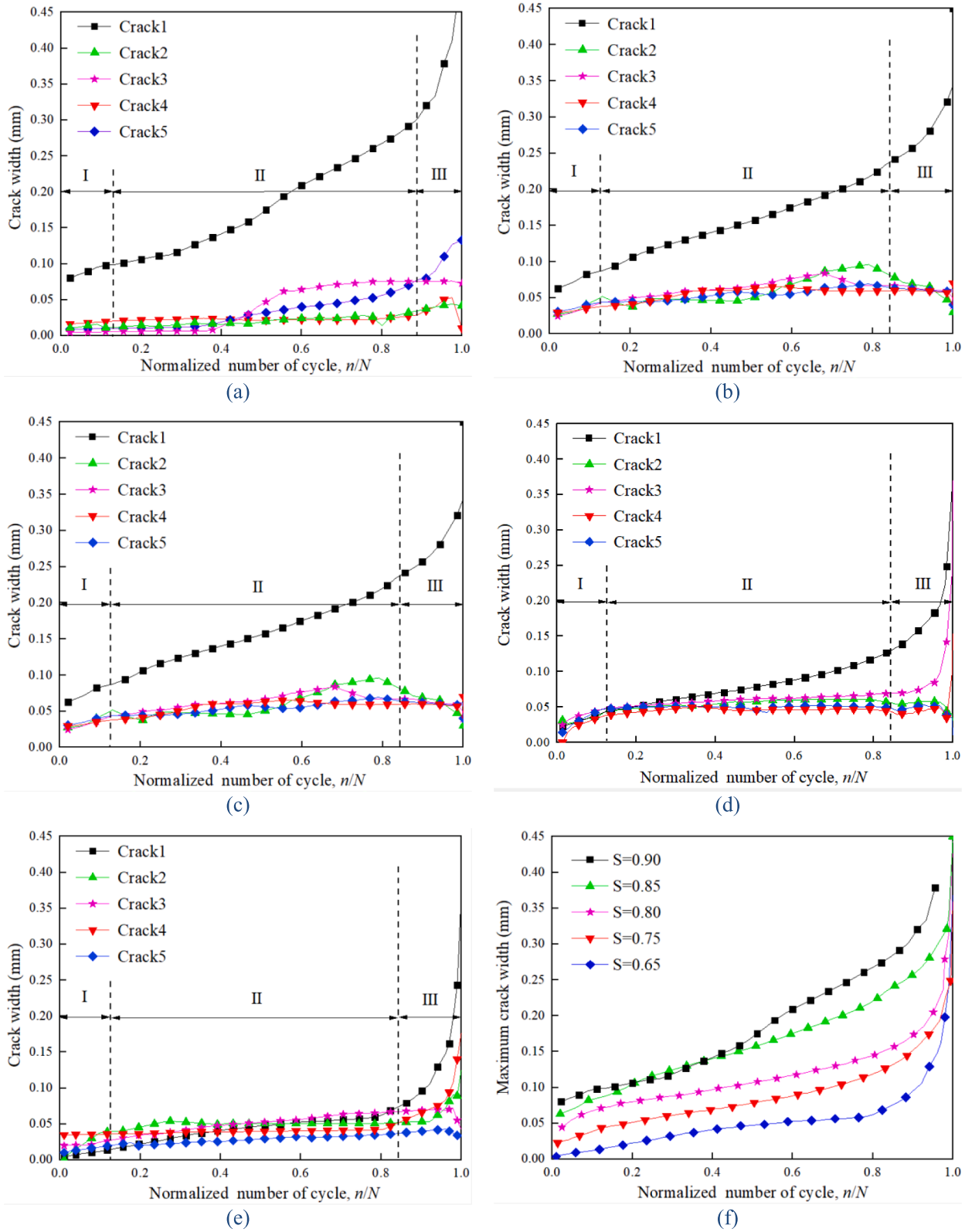

Fig. 15. Crack width evolution of selected 5 cracks along normalized number of cycle for each stress level: (a) $S = 0.9$; (b) $S = 0.85$; (c) $S = 0.8$; (d) $S = 0.75$; (e) $S = 0.65$. (f) comparison between the evolution maximum crack width.

stronger multiple cracking ability of ECC at higher stress level [51].

3.6. Evolution of the number of cracks under fatigue load

After the test, the number of cracks on the outermost surface under tension was counted. Fig. 12 shows the relationship between the averaged crack number and stress level. It is found that the number of cracks is proportional to the fatigue stress level. In the monotonic flexural test, more than 100 small cracks are formed in the ECC specimen. With stress level decreasing, less cracks were observed. The number of cracks

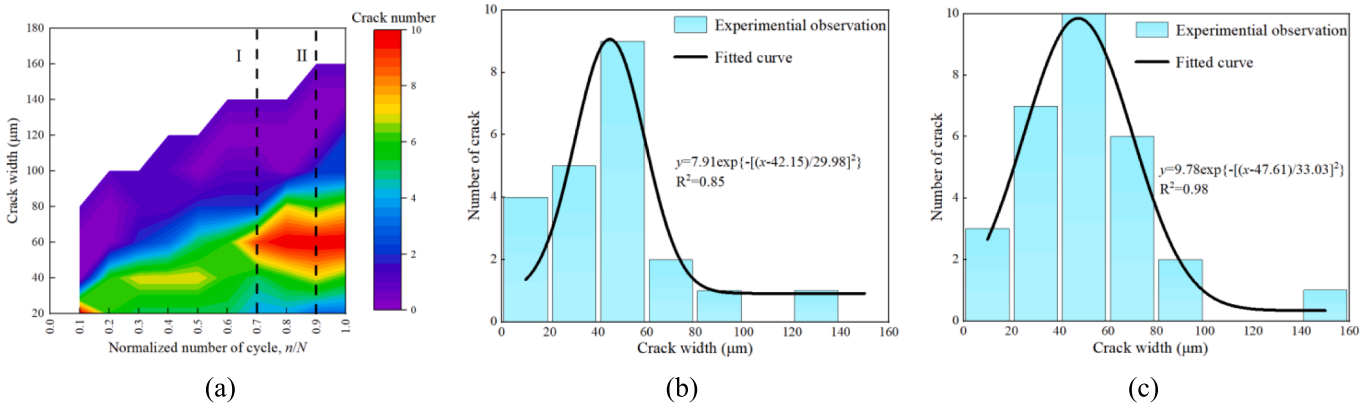

Fig. 16. Crack width distribution at the side for $S = 0.9$: (a) heat map of the crack width distribution; (b) fitting of the crack width distribution when n/N = 0.7; (b) fitting of the crack width distribution when n/N = 0.9.

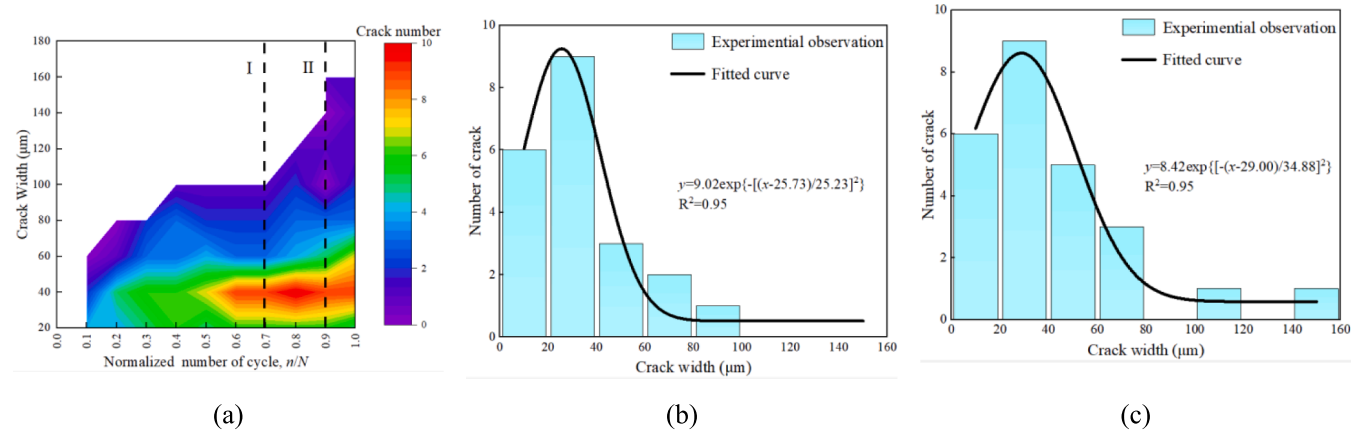

Fig. 17. Crack width distribution at the side for $S = 0.85$: (a) heat map of the crack width distribution; (b) fitting of the crack width distribution when n/N = 0.7; (b) fitting of the crack width distribution when n/N = 0.9.

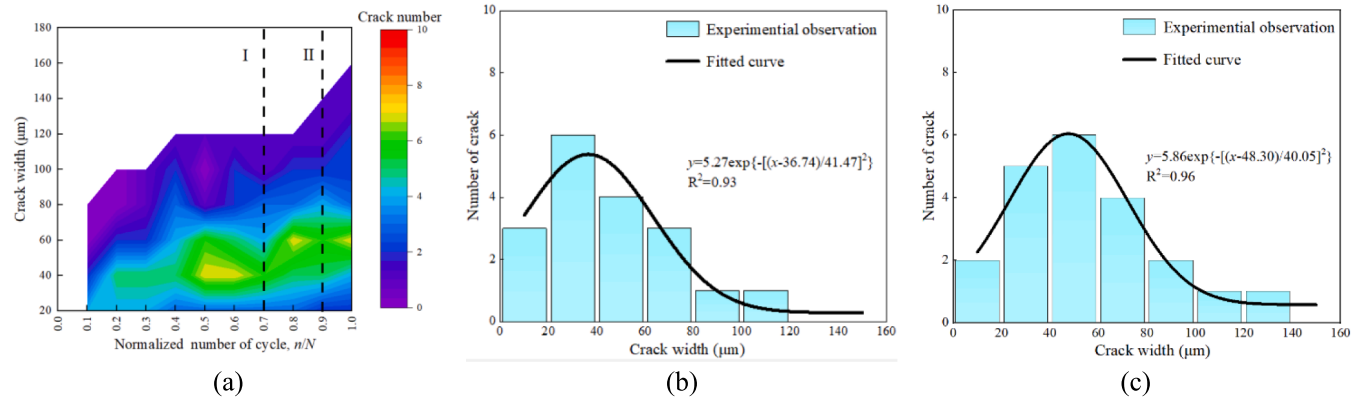

Fig. 18. Crack width distribution at the side for $S = 0.8$: (a) heat map of the crack width distribution; (b) fitting of the crack width distribution when n/N = 0.7; (b) fitting of the crack width distribution when n/N = 0.9.

decreases to 17 when a fatigue stress level of 0.65 is applied. This is because a stress intensity factor higher than the fracture toughness of matrix is required to form a new crack. Under the smaller fatigue stress level, the stress intensity factor is too low to form new cracks. Consequently, existing cracks keep extend and open with the load cycle. On this occasion, the fatigue resistance of the beam mainly relies on fatigue deterioration of fiber bridging ability on a few, or a single crack. A linear equation was used to fit the stress level-number of cracks relationship with a determination coefficient of 0.972. Similar observations have been reported in [16]. Furthermore, it should be noticed that the larger number of cracks formed in the specimens under higher stress level leads to the larger deflections during fatigue loading as shown in Fig. 10.

Evolution of the number of cracks at the side was derived from the DIC analysis and plotted against the normalized number of cycles under varying fatigue stress levels in Fig. 13. In line with the observations at the outmost surface under tension, much more cracks are found in the

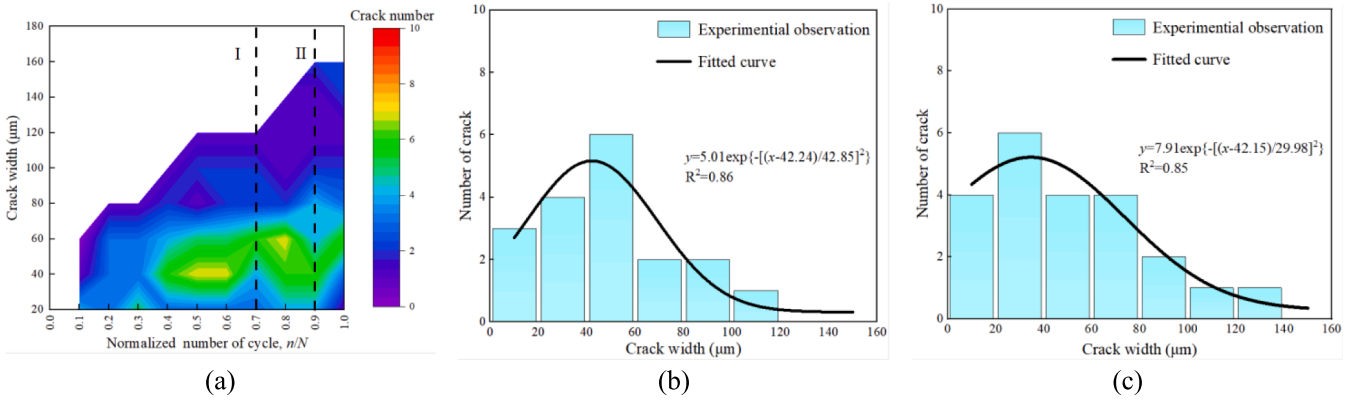

Fig. 19. Crack width distribution at the side for $S = 0.75$: (a) heat map of the crack width distribution; (b) fitting of the crack width distribution when n/N = 0.7; (b) fitting of the crack width distribution when n/N = 0.9.

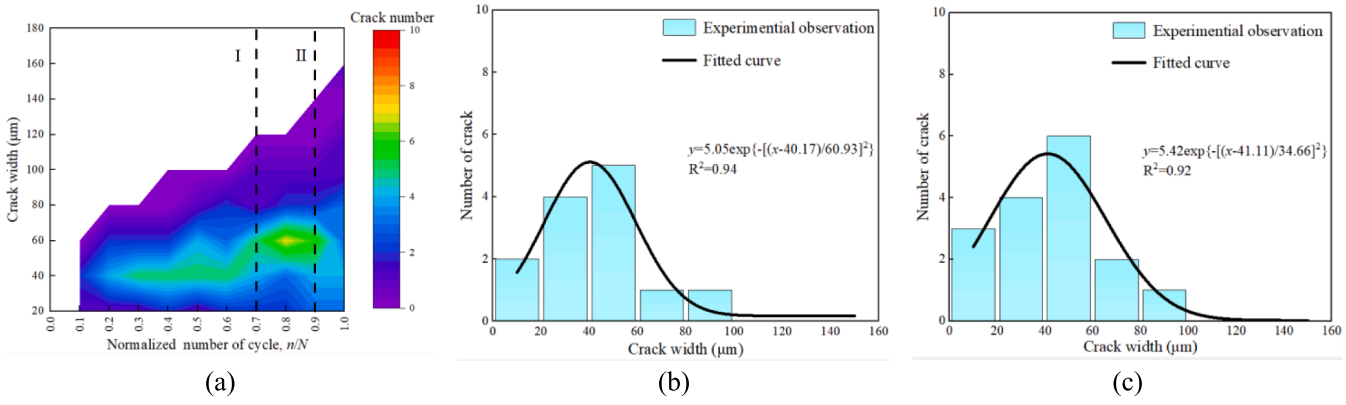

Fig. 20. Crack width distribution at the side for $S = 0.65$: (a) heat map of the crack width distribution; (b) fitting of the crack width distribution when n/N = 0.7; (b) fitting of the crack width distribution when n/N = 0.9.

Table 4
Two-dimension Gauss function fitting of the crack width distribution evolution.

Stress level, S	z_0	A	x_c	y_c	ω_1	ω_2	R^2
0.90	1.152	9.033	1.106	49.027	0.632	24.423	0.810
0.85	1.092	8.473	0.851	46.365	0.476	17.598	0.941
0.80	1.086	5.668	0.716	47.349	0.387	20.928	0.845
0.75	1.042	5.418	0.687	46.189	0.314	19.284	0.839
0.65	0.642	5.068	0.842	52.224	0.285	20.283	0.853

specimens under the higher fatigue load at the side. At failure state, 16 cracks had formed in $S = 0.65$ and 31 for $S = 0.90$, representing an almost 100 % increase. This trend also holds for specimens under the same normalized number of cycles. For example, the number of cracks is no more than 5 when the fatigue stress level is below 0.75 at the normalized number of cycles of 0.1. When $S = 0.9$, this number increases to 11, which is more than 100 % increase. Furthermore, regardless of the stress level, the number of cracks at the bottom propagating to the side surface increases with the normalized number of cycles. The increasing rate decreases the normalized number of cycles increasing. A power function ($y = ax^b$) is proposed to describe the relationship between the crack number and normalized number of cycles. The fitting results are presented in Table 3. Correlation coefficients are all above 0.96, indicating that the number of cracks is correlated with normalized number of cycles by power function for all stress levels. More interestingly, parameter a decreases with the fatigue stress level while b increases. It is worth mentioning that at the final phase, due to opening of the main crack, several narrow cracks reduce in width or even close. This leads to the decreased crack number that has been observed by DIC.

An observation of the fracture surface is presented in Fig. 14. It is shown that the fiber failure characteristics do not differ from those observed in the monotonic test. The fatigue life of ECC is determined by the combination of fiber rupture and fiber pull-out. At the low stress level ($S = 0.65$), most of the fibers are ruptured due to fatigue. In contrast, fibers are more likely to pull out from the matrix under high fatigue stress level ($S = 0.9$). This explains the greater mid-span defection, multiple cracking and crack opening ability of the ECC observed at the high stress level. Based on the fiber-bridging degradation, several models have been proposed to predict the *S-N* curves of ECC with great success [21,52,53].

3.7. Evolution of maximum crack under fatigue load

For each fatigue stress level, evolution of five cracks possessing the largest opening width was derived and shown in Fig. 15. Note that the crack opening measured from the DIC may differ from that obtained by LVDT: the LVDT measurement can only provide a sum of deformation over the gauge length in which multiple cracks and deformation of the uncracked area may be included. As it can be seen from Fig. 15, the three-stage mode is observed for the major crack causing the failure of the ECC specimen. In the initial phase, the monitored cracks open almost with the same rate. These cracks all contribute to the midspan deflection increment at the initial phase, see Fig. 10. In the second phase, one of these cracks opens with a relatively constant rate, while the width of the others almost remains unchanged. This is followed by a significant crack width increment of one or two cracks in the final phase. These cracks are the localized cracks that cause the failure of the specimen and contribute to the remarkable increase of the deflection in Fig. 10. Fig. 15f compares

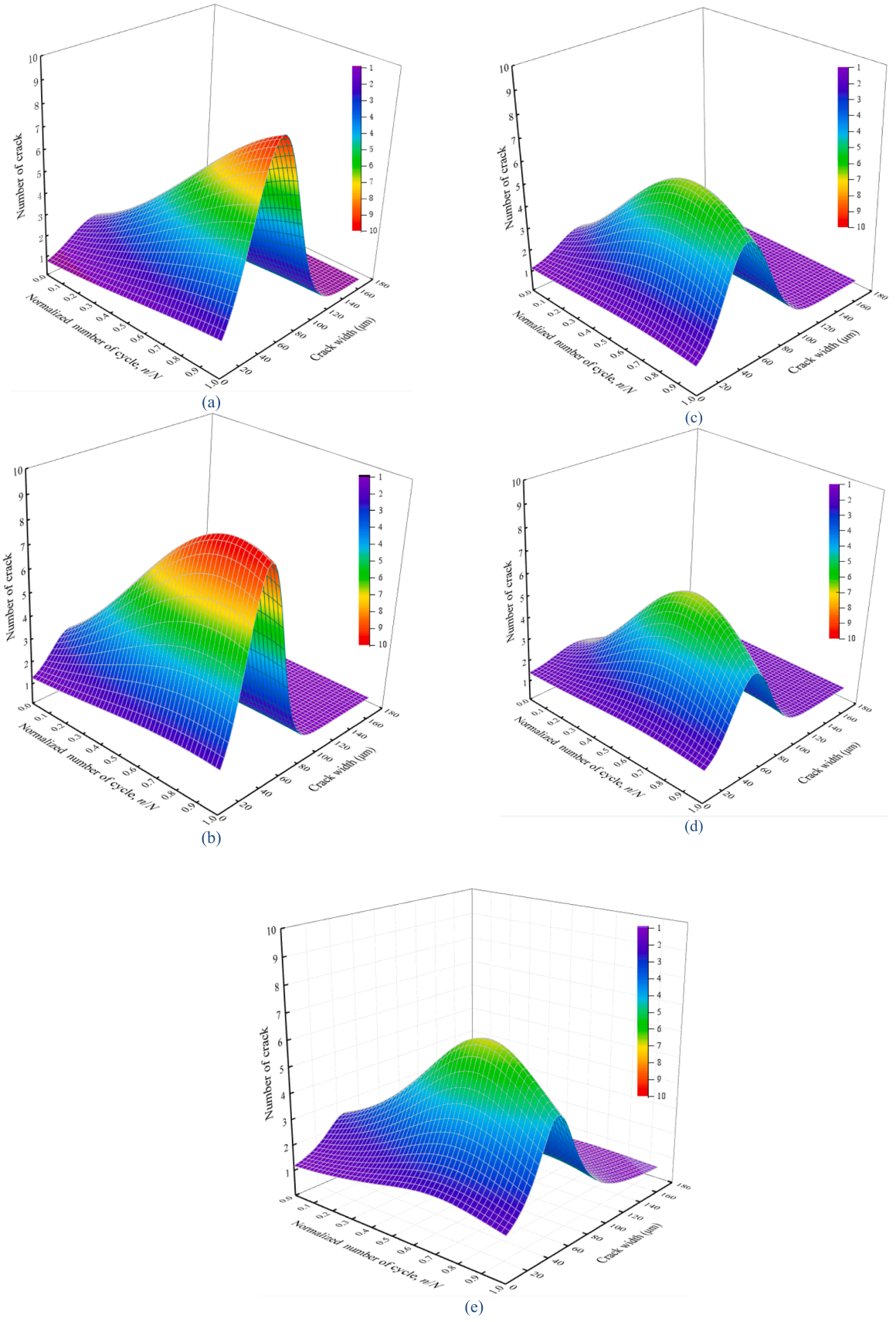

Fig. 21. Crack width distribution along with the normalized number of cycles for each stress level: (a) 0.9, (b) 0.85, (c) 0.8, (d) 0.75, (e) 0.65.

the maximum crack width evolution under various fatigue stress levels. It is clear that, at the initial phase, wider cracks form in the specimen under higher fatigue stress. In comparison to the ECC under low fatigue stress level ($S = 0.65$), the initial crack width is almost 10 times higher when high fatigue stress level ($S = 0.9$) is applied. In the second phase, the crack width growth rate is proportional to the fatigue stress level. The difference in crack width becomes largest at the end of the second phase where the maximum crack width under fatigue stress level of 0.9 reaches 0.3 mm and this number decreases to 0.2 mm for specimens under fatigue stress level of 0.65. In the final stage, unstable crack development is observed. When it comes to the final stage, greater crack width increment was found for the specimens under lower stress level. This is accompanied by the rapid deflection increase (see Fig. 10). Pearson's linear correlation coefficient, γ_{XY} [54] between the maximum crack opening width, X and midspan deflection Y was calculated.

$$\gamma_{XY} = \frac{\mathrm{cov}(X, Y)}{\omega_X \cdot \omega_Y} \tag{4}$$

where ω_X and ω_Y are the standard deviations of X and Y respectively, cov (X, Y) the covariance between X and Y. The calculated correlation coefficients are 0.9844, 0.9788, 0.9926, 0.9430 and 0.9775 for the fatigue stress levels of 0.9, 0.85, 0.8, 0.75 and 0.65 respectively. This means that there exists a strong linear relationship between the crack width and midspan deflection.

3.8. Evolution of crack width distribution under fatigue load

The observed evolutions of crack width distribution at the side for each stress level are presented in Figs. 16–20. The bin size was chosen as 20 μm, leading to 8 classes in the range between 0 and 160 μm. From the figures, one can observe that under cyclic loading, the crack widths at the side are centralized in between 20 and 80 μm. The crack width distributions corresponding to the normalized number of cycles of 0.7 and 0.5 were derived and fitted using the one-dimension Gauss function:

$$y = \mathrm{a}_1 e^{-\frac{(x-\mathrm{b}_1)^2}{\mathrm{c}_1^2}} \tag{5}$$

where x is the crack width at a certain normalized number of cycles, y the number of cracks corresponding to the crack width, a_1, b_1 and c_1 the fitted parameters. As can be seen from Figs. 16–20 all the determination coefficients are between 0.85 and 0.98. This indicates that the crack width distribution at a certain normalized number of cycles can be described well using the Gauss function. To correlate the crack number with the normalized number of cycles, a two-dimension Gauss function was applied:

$$z_1 = z_0 + Ae^{-\frac{(x_1-x_c)^2}{2\omega_1^2} - \frac{(y_1-y_c)^2}{2\omega_2^2}} \tag{6}$$

where x_1 represents the normalized recycle number, y_1 the crack width at a certain normalized number of cycles, z_1 the number of cracks corresponding to the crack width. z_0, A, x_c, y_c, ω_1, ω_2 are fitting parameters. A represents the amplitude. x_c and y_c determine the coordinate of the peak. ω_1 and ω_2 represent standard deviations.

Table 4 summarizes the calculated results. All the determination coefficients are above 0.8, indicating a strong correlation between crack width distribution and normalized number of cycles. When the stress level and normalized number of cycles are obtained, the crack width distribution can be estimated. This means that, with known cycle and stress level, it is possible to estimate the crack width distribution which offers basic data for the durability estimation [55–61]. The fitted crack width distributions are plotted in Fig. 21. It is clear that with the stress level increasing, the peak moves to the right, corresponding to a higher normalized number of cycles. This is attributed to the higher multiple cracking capacity of ECC at the higher stress level. The decrease of the crack number within the range between 20 and 80 μm can be attributed to the opening of the major crack which causes the closure of other narrow cracks. This phenomenon is more significant for specimens under lower fatigue stress level. Furthermore, it is interesting to notice that the peak crack width is close to 50 μm for all stress levels, with which the ECC should remain resistant to the penetration or diffusion of solutions containing aggressive ions [35,62–66].

4. Conclusions

The current article presents a study on fatigue life and cracking characterization of ECC under flexural cyclic load using digital image correlation technique. Based on the present results, the following conclusions can be drawn:

- A bilinear double logarithmic fatigue equation can describe the S-N relationship well. The fitted equation shows that when a stress level of 0.59 is applied, the fatigue life of ECC can reach 2×10^6 which agrees well with the observation in the literature.
- Fatigue life of ECC can be described by a double-parameter Weibull distribution. Most of the experimental results are within the failure probability between 5% and 95%.
- The applied stress level has a significant influence on the cracking behavior of ECC, which is closely linked to the deflection capacity. Three stages can be observed from the midspan deflection evolution as well as the maximum crack width evolution. A strong linear relationship exists between the crack width and the midspan deflection. The higher stress level leads to a greater midspan deflection which is accompanied by an increase in the number of cracks and the maximum crack width.
- A linear relationship is found in between the number of cracks on the tension face and fatigue stress at the failure stage. At the side surface, the evolution of number of cracks with respect to the normalized number of cycles can be described by a power function.
- Under fatigue loading, the major crack leading to the eventual failure of ECC initiates before the normalized number of cycles reaches 0.1. Under a low stress level, the major crack tends to propagate to the top rather than expanding the width, and the cracks are more localized. The multiple cracking ability of ECC gradually vanishes with the stress level decreasing.
- Regardless of the stress level, the crack widths at the side are centralized between 20 and 80 μm. Crack width distribution at a certain normalized number of cycles can be described well using the one-dimensional Gauss function. Two-dimensional Gauss function can be used to correlate the crack width distribution with normalized number of cycles. It shows that the peak crack width is around 50 μm. With the stress level increasing, this peak moves to the higher value of the normalized number of cycles.

The current study offers additional insight into the fatigue fracture behavior of ECC. The evolution of crack under fatigue loaded was continuously monitored using DIC, which provides a basis for durability assessment and design of ECC structures.

CRediT authorship contribution statement

Renjuan Sun: Methodology, Supervision, Writing – review & editing. **Lebing Han:** Investigation, Writing – original draft. **Hongzhi Zhang:** Funding acquisition, Methodology, Supervision, Writing – review & editing. **Zhi Ge:** Writing – review & editing. **Yanhua Guan:** Writing – review & editing. **Yifeng Ling:** Writing – review & editing. **Erik Schlangen:** Methodology, Writing – review & editing. **Branko Šavija:** Methodology, Writing – review & editing.

Declaration of Competing Interest

The authors declare that they have no known competing financial

interests or personal relationships that could have appeared to influence the work reported in this paper.

Acknowledgements

This work was supported by the National Natural Science Foundation of China (No.52008234, 51978387, 51478252), Taishan Scholars Foundation of Shandong Province (No. tsqn201909032), Key Technology Research and Development Program of Shandong (2015GSF122009) and Natural Science Foundation of Jiangsu Province (No. BK20200235).

References

[1] A. Bentur, S. Mindess, Fibre reinforced cementitious composites, CRC Press, 2006.
[2] V.C. Li, From micromechanics to structural engineering the design of cementitious composites for civil engineering applications, Doboku Gakkai Ronbunshu 1993 (471) (1993) 1–12.
[3] V.C. Li, S. Wang, C. Wu, Tensile Strain-Hardening Behavior of Polyvinyl Alcohol Engineered Cementitious Composite (PVA-ECC), ACI Mater. J. 98 (6) (2001).
[4] V.C. Li, On engineered cementitious composites (ECC). A review of the material and its applications, J. Adv. Concr. Technol 1 (3) (2003) 215–230.
[5] C.W.S.W.A.O. Victor C. Li, S. Tadashi, Interface Tailoring for Strain-Hardening Polyvinyl Alcohol-Engineered Cementitious Composite (PVA-ECC), ACI Mater. J. 99(5).
[6] M. Maalej, V.C. Li, Flexural/Tensile Strength Ratio in Engineered Cementitious, Composites 6 (4) (1994) 513–528.
[7] V.C. Li, Engineered Cementitious Composites (ECC): Bendable Concrete for Sustainable and Resilient Infrastructure, Springer, Berlin, Germany, 2019.
[8] Y. Yang, M.D. Lepech, E.-H. Yang, V.C. Li, Autogenous healing of engineered cementitious composites under wet–dry cycles, Cem. Concr. Res. 39 (5) (2009) 382–390.
[9] S. Qian, J. Zhou, M.R. de Rooij, E. Schlangen, G. Ye, K. van Breugel, Self-healing behavior of strain hardening cementitious composites incorporating local waste materials, Cem. Concr. Compos. 31 (9) (2009) 613–621.
[10] S.Z. Qian, J. Zhou, E. Schlangen, Influence of curing condition and precracking time on the self-healing behavior of Engineered Cementitious Composites, Cem. Concr. Compos. 32 (9) (2010) 686–693.
[11] Y. Yang, E.-H. Yang, V.C. Li, Autogenous healing of engineered cementitious composites at early age, Cem. Concr. Res. 41 (2) (2011) 176–183.
[12] J. Zhang, V.C. Li, Monotonic and fatigue performance in bending of fiber-reinforced engineered cementitious composite in overlay system, Cement and Concrete Research 32 (3) (2002) 415–423.
[13] P. Suthiwarapirak, T. Matsumoto, T. Kanda, Multiple Cracking and Fiber Bridging Characteristics of Engineered Cementitious Composites under Fatigue Flexure, J. Mater. Civil Eng. 16 (5) (2004) 433–443.
[14] H. Huang, X. Gao, L. Teng, Fiber alignment and its effect on mechanical properties of UHPC: An overview, Constr. Building Materials 296 (2021), 123741.
[15] P. Suthiwarapirak, T. Matsumoto, T. Kanda, Flexural fatigue failure characteristics of an engineered cementitious composite and polymer cement mortars, Doboku Gakkai Ronbunshu 2002 (718) (2002) 121–134.
[16] T. Matsumoto, P. Suthiwarapirak, T. Kanda, Mechanisms of Multiple Cracking and Fracture of DFRCC under Fatigue Flexure, J. Adv. Concrete Technol. 1 (3) (2003) 299–306.
[17] S. Müller, V. Mechtcherine, Fatigue behaviour of strain-hardening cement-based composites (SHCC), Cem. Concr. Res. 92 (2017) 75–83.
[18] Q. Li, B. Huang, S. Xu, B. Zhou, R.C. Yu, Compressive fatigue damage and failure mechanism of fiber reinforced cementitious material with high ductility, Cem. Concr. Res. 90 (2016) 174–183.
[19] B.-T. Huang, Q.-H. Li, S.-L. Xu, B.-M. Zhou, Frequency Effect on the Compressive Fatigue Behavior of Ultrahigh Toughness Cementitious Composites: Experimental Study and Probabilistic, Analysis 143 (8) (2017) 04017073.
[20] B.-T. Huang, Q.-H. Li, S.-L. Xu, W. Liu, H.-T. Wang, Fatigue deformation behavior and fiber failure mechanism of ultra-high toughness cementitious composites in compression, Materials & Design 157 (2018) 457–468.
[21] J. Qiu, E.-H. Yang, Micromechanics-based investigation of fatigue deterioration of engineered cementitious composite (ECC), Cem. Concr. Res. 95 (2017) 65–74.
[22] J. Qiu, E.-H. Yang, A micromechanics-based fatigue dependent fiber-bridging constitutive model, Cem. Concr. Res. 90 (2016) 117–126.
[23] J. Qiu, X.-N. Lim, E.-H. Yang, Fatigue-induced deterioration of the interface between micro-polyvinyl alcohol (PVA) fiber and cement matrix, Cem. Concr. Res. 90 (2016) 127–136.
[24] W. Liu, S. Xu, P. Feng, Fatigue damage propagation models for ductile fracture of ultrahigh toughness cementitious composites, IJDM 26 (6) (2016) 919–932.
[25] W. Liu, S. Xu, H. Li, Flexural fatigue damage model of ultra-high toughness cementitious composites on base of continuum damage mechanics, IJDM 23 (7) (2014) 949–963.
[26] S. Xu, W. Liu, Investigation on crack propagation law of ultra-high toughness cementitious composites under fatigue flexure, Eng. Fracture Mech. 93 (2012) 1–12.
[27] B.-T. Huang, Q.-H. Li, S.-L. Xu, Fatigue Deformation Model of Plain and Fiber-Reinforced Concrete Based on Weibull Function, J. Struct. Eng. 145 (1) (2019) 04018234.
[28] S. Das, M. Aguayo, V. Dey, R. Kachala, B. Mobasher, G. Sant, N. Neithalath, The fracture response of blended formulations containing limestone powder: Evaluations using two-parameter fracture model and digital image correlation, Cem. Concr. Compos. 53 (2014) 316–326.
[29] Y. Xu, H. Zhang, E. Schlangen, M. Luković, B. Šavija, Cementitious cellular composites with auxetic behavior, Cem. Concr. Compos. 111 (2020).
[30] Y. Chen, K. Jansen, H. Zhang, C. Romero Rodriguez, Y. Gan, O. Çopuroğlu, E. Schlangen, Effect of printing parameters on interlayer bond strength of 3D printed limestone-calcined clay-based cementitious materials: An experimental and numerical study, Constr. Build. Mater. 262 (2020).
[31] R. Ranade, J. Zhang, J.P. Lynch, V.C. Li, Influence of micro-cracking on the composite resistivity of Engineered Cementitious Composites, Cem. Concr. Res. 58 (2014) 1–12.
[32] M. Ohno, V.C. Li, A feasibility study of strain hardening fiber reinforced fly ash-based geopolymer composites, Constr. Build. Mater. 57 (2014) 163–168.
[33] Z. Ge, A.M. Tawfek, H. Zhang, Y. Yang, H. Yuan, R. Sun, Z. Wang, Influence of an extrusion approach on the fiber orientation and mechanical properties of engineering cementitious composite, Construction and Building Materials 306 (2021), 124876.
[34] M. Luković, D. Hordijk, Z. Huang, E. Schlangen, Strain Hardening Cementitious Composite (SHCC) for crack width control in reinforced concrete beams, Heron 64 (1/2) (2019) 181.
[35] R. Sun, X. Hu, Y. Ling, Z. Zuo, P. Zhuang, F. Wang, Chloride diffusion behavior of engineered cementitious composite under dry-wet cycles, Constr. Build. Mater. 260 (2020), 119943.
[36] L.-P. Guo, W. Sun, X.-Y. He, Z.-B. Xu, Application of DSCM in prediction of potential fatigue crack path on concrete surface, Engineering Fracture Mechanics 75 (3) (2008) 643–651.
[37] N. Gehri, J. Mata-Falcón, W. Kaufmann, Automated crack detection and measurement based on digital image correlation, Constr. Build. Mater. 256 (2020), 119383.
[38] X. Shen, E. Brühwiler, Influence of local fiber distribution on tensile behavior of strain hardening UHPFRC using NDT and DIC, Cem. Concr. Res. 132 (2020), 106042.
[39] I.M.G. Bertelsen, C. Kragh, G. Cardinaud, L.M. Ottosen, G. Fischer, Quantification of plastic shrinkage cracking in mortars using digital image correlation, Cem. Concr. Res. 123 (2019), 105761.
[40] Y. Niu, H. Huang, J. Zhang, W. Jin, J. Wei, Q. Yu, Development of the strain field along the crack in ultra-high-performance fiber-reinforced concrete (UHPFRC) under bending by digital image correlation technique, Cem. Concr. Res. 125 (2019), 105821.
[41] T. Mauroux, F. Benboudjema, P. Turcry, A. Aït-Mokhtar, O. Deves, Study of cracking due to drying in coating mortars by digital image correlation, Cem. Concr. Res. 42 (7) (2012) 1014–1023.
[42] Y. Wang, J. Jiang, C. Wanintrudal, C. Du, D. Zhou, L.M. Smith, L. Yang, Whole field sheet-metal tensile test using digital image correlation, Experimental Techniques 34 (2) (2010) 54–59.
[43] D.T.K. John S. Lawler, P.S. Surendra, Measuring Three-Dimensional Damage in Concrete under Compression, ACI Mater. J. 98(6).
[44] G. Ruocci, C. Rospars, G. Moreau, P. Bisch, S. Erlicher, A. Delaplace, J.-M. Henault, Digital Image Correlation and Noise-filtering Approach for the Cracking Assessment of Massive Reinforced Concrete Structures, Strain 52 (6) (2016) 503–521.
[45] B.H. Oh, Fatigue Analysis of Plain Concrete in Flexure, J. Struct. Eng. 112 (2) (1986) 273–288.
[46] H. Li, M.-H. Zhang, J.-P. Ou, Flexural fatigue performance of concrete containing nano-particles for pavement, IJFa 29 (7) (2007) 1292–1301.
[47] O. Byung Hwan, Fatigue Life Distributions of Concrete for Various Stress Levels, ACI Mater. J. 88(2).
[48] A. Medeiros, X. Zhang, G. Ruiz, R.C. Yu, M.d.S.L. Velasco, Effect of the loading frequency on the compressive fatigue behavior of plain and fiber reinforced concrete, IJFa 70 (2015) 342–350.
[49] L. Saucedo, R.C. Yu, A. Medeiros, X. Zhang, G. Ruiz, A probabilistic fatigue model based on the initial distribution to consider frequency effect in plain and fiber reinforced concrete, IJFa 48 (2013) 308–318.
[50] Y. Gan, H. Zhang, Y. Zhang, Y. Xu, E. Schlangen, K. van Breugel, B. Šavija, Experimental study of flexural fatigue behaviour of cement paste at the microscale, IJFa 151 (2021), 106378.
[51] W. Liu, L. Luo, S. Xu, H. Zhao, Effect of fiber volume fraction on crack propagation rate of ultra-high toughness cementitious composites, Eng. Fracture Mech. 124 (2014) 52–63.
[52] P. Suthiwarapirak, T. Matsumoto, Fiber bridging degradation based fatigue analysis of ECC under flexure, J. Appl. Mech. 6 (2003) 1179–1188.
[53] T. Matsumoto, Crack bridging law in discontinuous fiber reinforced composites under cyclic loadin, J. Appl. Mech. 10 (2007) 923–933.
[54] P. Sedgwick, Pearson's correlation coefficient, Bmj 345 (2012).
[55] D. Wang, Q. Wang, Z. Huang, New insights into the early reaction of NaOH-activated slag in the presence of CaSO4, Composites Part B: Engineering 198 (2020), 108207.
[56] S. Zhuang, Q. Wang, Inhibition mechanisms of steel slag on the early-age hydration of cement, Cement and Concrete Research 140 (2021), 106283.
[57] B. Šavija, J. Pacheco, E. Schlangen, Lattice modeling of chloride diffusion in sound and cracked concrete, Cem. Concr. Compos. 42 (2013) 30–40.

[58] B. Šavija, H. Zhang, E. Schlangen, Assessing Hydrated Cement Paste Properties Using Experimentally Informed Discrete Models, J. Mater. Civ. Eng. 31 (9) (2019) 04019169.
[59] T. Vidal, A. Castel, R. François, Analyzing crack width to predict corrosion in reinforced concrete, Cem. Concr. Res. 34 (1) (2004) 165–174.
[60] M.B. Otieno, M.G. Alexander, H.-D. Beushausen, Corrosion in cracked and uncracked concrete – influence of crack width, concrete quality and crack reopening, Magazine Concr. Res. 62 (6) (2010) 393–404.
[61] Z. Mo, X. Gao, A. Su, Mechanical performances and microstructures of metakaolin contained UHPC matrix under steam curing conditions, Constr. Building Mater. 268 (2021), 121112.
[62] M.D. Lepech, V.C.J.C. Li, C. Composites, Water permeability of engineered cementitious composites, Cement Concr. Compos. 31 (10) (2009) 744–753.
[63] M. Sahmaran, M. Li, V.C. Li, Transport properties of engineered cementitious composites under chloride exposure, ACI Mater. J. 104 (6) (2007) 604–611.
[64] K.J. Wang, D.C. Jansen, S.P. Shah, A.F. Karr, Permeability study of cracked concrete, Cem. Concr. Res. 27 (3) (1997) 381–393.
[65] C.-L. Zhang, W.-K. Chen, S. Mu, B. Šavija, Q.-F. Liu, Numerical investigation of external sulfate attack and its effect on chloride binding and diffusion in concrete, Constr. Build. Mater. 285 (2021), 122806.
[66] Q.-F. Liu, M.F. Iqbal, J. Yang, X.-Y. Lu, P. Zhang, M. Rauf, Prediction of chloride diffusivity in concrete using artificial neural network: Modelling and performance evaluation, Constr. Build. Mater. 268 (2021), 121082.